

Magnetohydrodynamic Control of Interfacial Degradation in Lithium-ion Batteries for Fast Charging Applications

Abhishek Sarkar,[†] Pranav Shrotriya,[‡] and Ikenna C. Nlebedim^{†,}*

[†]Ames Laboratory of US Department of Energy, Ames, IA – 50011, USA

[‡]Department of Mechanical Engineering, Iowa State University, Ames, IA – 50011, USA

Keywords: magneto-electrochemical, electromagnetism, magnetohydrodynamic force, fast charging, film deposition, lithium-ion battery

ABSTRACT: Interfacial anodic degradation in graphitic materials under fast charging conditions causes severe performance loss and safety hazard in lithium ion batteries. We present a novel method for minimizing the growth of these ageing mechanism by application of an external magnetic field. Under magnetic field, paramagnetic lithium ions experience a magnetohydrodynamic force, which rotates the perpendicularly diffusing species and homogenizes the ionic transport. This phenomenon minimizes the overpotential hotspots at the anode/separator interface, consequently reducing SEI growth, lithium plating, and interfacial fracture. *In-situ* electrochemical measurements indicate an improvement in capacity for lithium cobalt oxide/graphite pouch cell (20 mAh) charged from 1 – 5 C under an applied field of 1.8 kG, with a maximum capacity gain of 22% at 5C. Post-mortem FE-SEM and EDS mapping shows that samples charged with magnetic field have a reduced lithium deposition at 3C and a complete suppression of interfacial fracture at 5C. At 5C, a 24% reduction in the lithium content is observed by performing XPS on the anodic interfacial film. Finally, fast charging performance under variable magnetic field strengths indicate a saturation behavior in capacity at high fields (> 2 kG), thereby limiting the field and consequent energy requirements to obtain maximum capacity gain under extreme conditions.

1. INTRODUCTION

Lithium-ion batteries (LIBs) that are capable of fast charging with reliable cyclic performance and long service life, can provide a sustainable energy storage solution for the automobile and consumer electronics applications¹⁻³. Graphite is the most widely used commercial anode material with the global market of almost US\$1 billion in 2019. The market is forecasted to exceed US\$1.9 billion by 2024⁴. The layered crystalline structure of graphite anodes allows lithium ions to intercalate between the stacks of graphene sheets. However, under fast charging conditions, lithium-ion batteries are subject to severe performance degradation resulting from the formation of the solid-electrolyte interface (SEI), lithium plating on graphite anodes and film fractures. These aging mechanisms lead to capacity loss, low columbic efficiency, increased propensity for thermal runaway, and/or severe structural damage to the electrode⁵.

The ionically conducting but electronically insulating SEI layers are composed of lithium salts (organic and inorganic) which form when the anode's redox potential lies outside the potential range of the battery⁶⁻⁹. During progressive cycling of the battery, the slow kinetics of the graphite anode leads to capacity loss due to the slow but continued evolution of the SEI layer that irreversibly consumes the active material and increases the anodic surface's resistance^{10,11}.

During fast charging, the separator membrane's convoluted diffusion pathways lead to non-uniform ionic flux and irregular hotspots of lithium concentration on the anode/separator interface. This leads to the onset of two severely deteriorating mechanisms at interfacial surface, i.e. lithium plating and film fracture. Graphite anodes are especially susceptible to metallic lithium plating due to the lower operating open-circuit voltage (OCV) range ($\sim 1.0 - 0.01$ V)¹². The localized spikes in lithium concentration causes a rapid anodic potential decay¹³, and the overpotential becomes < 0 V (vs. Li/Li⁺) leading to electrodeposition of metallic lithium at anode/separator interface^{5,14,15}.

Ultra-high-precision coulometric and calorimetric measurements, as well as post mortem SEM imaging, reveal that the lithium plating mechanism results in rapid decay of cell capacity^{16–18}. In addition to the capacity loss, uncontrolled dendritic lithium growth could pierce the separator membrane leading to thermal runaway due to short-circuit between the electrodes – a safety concern. Another consequence of rapid lithiation is mechanical stresses induced on the electrode surfaces due to volumetric expansion (~10.3%). The cyclic expansion of the electrode causes fatigue crack formation, which exposes new electrode surface to electrolyte which, in turn, contributes to SEI film evolution and loss of active lithium through repeated fracture and formation cycles^{19–22}.

We present an approach that utilizes externally applied magnetic fields for limiting lithium plating and interfacial fracture in graphite anode during fast charging of lithium batteries (Figure 1). The electric field creates a net motion of the lithium ions to diffuse between the electrodes. Although the bulk ensemble diffusion occurs from cathode to anode, the individual ionic species exhibit random motion due to the convoluted diffusion pathways in the electrode²³ and separator membrane²⁴. These randomly moving species create lithium hotspots at the anode/separator interface creating conditions to initiate interfacial degradation. Ionic transport (flux, j) under magnetic field (B) leads to magnetohydrodynamic (MHD) or Lorentz force interactions (F_{MHD})^{25–27}.

$$F_{MHD} = q(v \times B) = j \times B \quad (1)$$

The lithium-ions traversing (charge and velocity, q and v) parallel (or antiparallel) to the applied field's direction experience no MHD forces ($v \times B = 0$) (Figure 1C). However, ionic flux transverse (or angular) to the magnetic field is subjected to convective MHD forces causing a rotation of the ionic flux (vortex) normal to the diffusion and field direction (Figure 1C). Hence,

the external magnetic field parallel to the normal vector of the separator should improve the electrolyte's diffusion capabilities and increase the homogeneity of charge distribution over the anode surface. Previous works have focused on application of MHD in lithium metal batteries for uniform lithium deposition^{28,29} and MHD interactions as a technique for characterization³⁰. Due to the inherent morphology and physicochemical behavior of graphite anodes, the application of MHD to limit interfacial degradation provides a facile route for fast charging.

In this work, we investigate if the increased homogeneity of ionic flux, due to applied magnetic field, will suppress the formation of lithium concentration hot-spots on the anode surface and thus, minimize the capacity loss and electrode damage associated with fast charging. These force interactions are exploited to regularize the lithium flux (Figure 1). In-situ and post-mortem characterization of the morphology and chemistry of the interfacial degradation film are undertaken to reveal the effect of the MHD forces during extreme fast charging conditions. Finally, optimizations based on magnetic field strength on the evolution of physicochemical properties of the pouch cells during fast charging are performed to achieve the maximum performance gain.

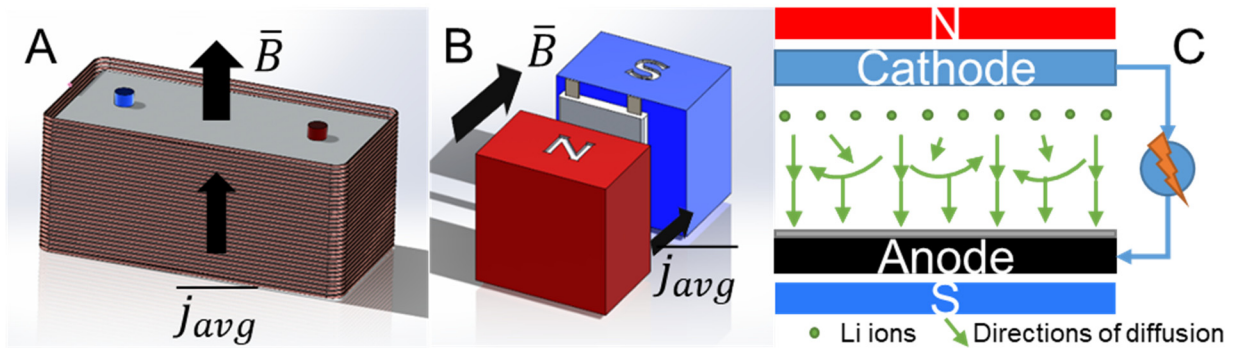


Figure 1. Schematic representation of magnetohydrodynamics during fast charging of conventional LIBs. (A and B) Schematic representation of lithium-ion battery under the application of external magnetic field with electromagnet (A) and permanent magnet (B). \bar{B} is the

magnetic field vector and $\overline{J_{avg}}$ is the ensemble average lithium ion flux vector. (C) Schematic of MHD forces creating a convective current on non-uniform lithium ion fluxes during fast charging under applied magnetic field.

2. EXPERIMENTAL PROCEDURES

2.1. Electrochemical Analysis

Lithium cobalt oxide/graphite pouch cells with a nominal capacity of 20 mAh (PowerStream GM201515) were cycled using an MTI BST8-300 mA battery testing station. The pouch cells have been formerly tested for reliability and stability by manufacturer, including altitude simulation, thermal, vibration, shock, external short circuit, crushing and forced discharge³¹. The pouch cells are composed of multiple layers of alternate cathode, separator and anode. All pouch cells were initialized by discharging at constant current (CC) with C/10 till 3.0 V, CC charging till 90% state of charge (SOC), and CC discharging till 3.0 V. The pouch cells were left to rest for 30 min after each charge/discharge half cycle. After initializing, the following protocol was followed for fast charging of the pouch cells. CC charge till 4.2 V at desired C-rate (1 – 5 C), CV till 90% SOC, rest for 30 min, CC discharge till 3.0 V, and rest for 30 min. This protocol was repeated for 10 cycles. The DCR measurements were performed at the end of each rest period after fast charging. The DCR measurements are performed by the in-built protocol of the battery charging station, wherein a small current is applied (<10% of rated) and the potential response is measured. The resistance is calculated using, $DCR = \Delta V / \Delta I$. The measured DCR with cycles was adjusted by subtracting the DCR at the slow charging cycle to obtain the DCR variation due to film growth. The pouch cell temperature was closely monitored using an in-built thermocouple with the battery testing station.

2.2. Magnetic field source

Magnetic field was applied using a C-core electromagnet (EM). The core material was CR-1010 steel and the windings were AWG22 coated copper wire with 3500 turns. A Kepco KLN-1500 power source was used to modulate the DC current. The B-field of the EM coil was measured using a FW Bell 5080 gaussmeter. As a reference, $1000\text{ G} = 1\text{ kG}$ and $1\text{ T} = 10\text{ kG}$.

2.3. Disassembly and thickness measurement

The pouch cells were discharge @ CC till 2.7 V and held at CV till C/20. The cells were quickly transferred into a glovebox (MBraun, $< 0.1\text{ ppm O}_2$ and H_2O)³² where they were cut open and the electrodes were carefully separated without damaging the deposited films. The film thickness was measured using a Mitutoyo IP65 micrometer with least count of $1\text{ }\mu\text{m}$. The samples were always stored inside the glovebox in airtight vials to prevent oxidation.

2.4. FE-SEM/EDS analyses

FE-SEM and EDS analyses were performed using a FEI Teneo LoVac field-emission scanning electron microscope. The samples were transported from the glovebox for the analyses using a specialized vacuum sample holder and were only opened under high vacuum inside the SEM. Both secondary electron and backscattered electron imaging were performed using a 5 kV electron beam. The backscattered image showed a better contrast in the film vs. graphite phases.

2.5. X-ray photoelectron studies

XPS was performed using an Amicus XPS system. The samples were transferred in a specialized holder from the glovebox to the XPS unit. Argon sputtering was used to etch the film to perform depth profiling. The survey spectra were deconvoluted using CASAXPS to get the atomic percentage of the interfacial film.

3. RESULTS AND DISCUSSION

3.1. Electrochemical analysis of magneto-electrochemical interactions during fast charging.

To realize the effect of the MHD force on the interfacial degradation kinetics of fast charging lithium-ion batteries, commercial, full LCO/C pouch cells (20mAh, rated capacity) were charged from 1C to 5C over 10 cycles at room temperature (298 K) both without ($B = 0$ kG) and with magnetic field ($B = 1.8$ kG). At 1C the capacity fade is not significant over the 10 cycles as shown in Figure 2A. However, the capacity fade increases considerably with an increase in charging rate (Figure S1A-C) and is found to be maximum at 5C (Figure 2B). Low capacity fade at low charging rates (1C) indicates a slow and uniform lithium flux distribution, leading to insignificant lithium plating. An increased capacity fade and voltage relaxation plateau (Figure S1D) at charging rates $\geq 2C$ suggest the onset of degradation due to lithium plating. Fast charging induces severe concentration gradients within the electrode due to diffusion limitations. Moreover, the lithium stripping mechanism from 2C onwards induces additional lithium flux which alters the surface concentration. The 2C sample has a lower OCV than 1C (Figure S1D) because of larger concentration gradient, which causes 2C to equilibrate at a lower OCV (or SOC) than the latter. The OCV systematically increases from 2C to 5C due to additional lithium flux from the lithium stripping and re-intercalation processes. This additional lithium available for intercalation increases the SOC (and thereby the OCV). A sharp depreciation in the coulombic efficiency in the initial charging cycles at higher charging rates indicates a significant lithium inventory loss during lithium plating. A revival of the coulombic efficiency was observed beyond second cycle which is surmised to be caused by a rapid SEI formation on the plated lithium. It is hypothesized that the SEI layer encapsulates the plated lithium, thereby creating a potential barrier and minimizing further lithium deposition.

Fast charging the pouch cells under magnetic field resulted in a higher discharge capacity as shown in Figure 2B, indicating lower loss of active lithium inventory from the degradation

mechanisms. The gain in discharge capacity under the magnetic field ($Q_{gain} = (Q_D|_{field} - Q_D|_{no\ field})/Q_D|_{no\ field}$), (1 – 5 C) under magnetic field is plotted in Figure 2C. An increasing magnitude of capacity gain is observed with increase in charging rates. The MHD increases with C-rate due to more lithium flux with transverse velocity being available for homogenization with magnetic field at higher C-rates. This is because of a) C-rate \propto lithium-ion flux (j), thus increasing F_{MHD} in Equation 1, and b) at higher C-rates, the non-homogeneity in the ion flux increases, leading to larger transverse velocity. This effect causes mini vortices of lithium ions, consequently homogenizing lithium concentration at the anode/separator interface. A maximum capacity gain of 22% is observed at 5C charging under 1.8 kG field. The observed capacity gain can substantially reduce the potential for sudden failure, thus promoting cycle life.

The DC resistance (DCR) at the end of the rest period after fast charging without magnet field showed a sharp depreciation in the initial cycles of fast charging, followed by a gradual rise (Figure S1E). The initial depreciation of DCR indicates the deposition of an electrically conductive material, like metallic lithium under fast charging, reducing the cell resistance. The increase in the DCR over subsequent cycles suggests the formation of a thick electrically insulating layer, like the SEI layer, over the conductive lithium metal. The cells undergoing fast charging under an external magnetic field show considerably reduced DCR loss (Figure S1F). Figure 2D shows the differences in magnitude of DCR losses with and without magnetic field. The differences in DCR loss increases with C-rates, indicating a reduction in the metallic lithium deposition. The increase in capacity gain and reduced DCR loss with increased charging rates indicate that fast charging under magnetic field reduces interfacial degradation. In all the electrochemical analysis, the pouch cell temperature did not fluctuate more than $\pm 1^\circ\text{C}$ (Figure S1G).

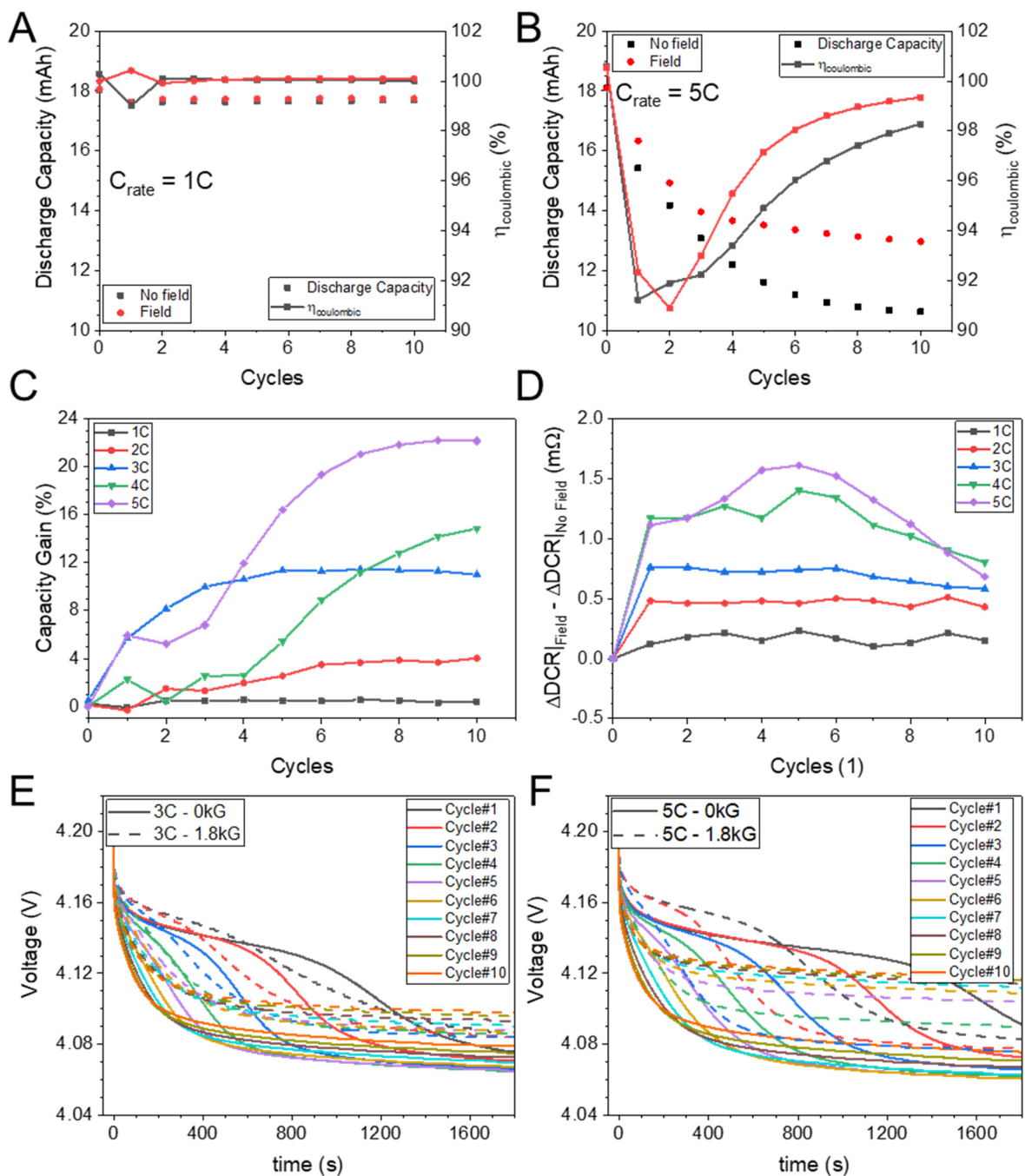


Figure 2. Electrochemical analyses showing the effect of magnetic field ($B = 1.8\text{ kG}$) on 20mAh LCO/C pouch cells over 10 cycles. (A and B) Discharge capacity and coulombic efficiency of pouch cells over multiple charging rates varying from 1C (A) and 5C (B). (C) Capacity gain over 1 – 5 C due to application of magnetic field. (D) ΔDCR from with/without applied field during

rest period after fast charging. (E and F) Voltage relaxation analysis of pouch cells charged with and without magnetic field over 10 cycles charged at 3C (E) and 5C (F).

The relaxation voltage plateau at 3C and 5C of the pouch cells charged under magnetic field indicate a definitive suppression in the plating mechanism over multiple cycles (Figures 2E and 2F). The voltage plateau receded in both cases on application of magnetic field, suggesting reduced lithium stripping re-intercalation, and consequently reduced plating. Moreover, the width of the plateau is suppressed under the influence of field, further supporting the reduction in the interfacial degradation. The voltage plateau was fully suppressed by Cycle#6 and Cycle#5 for the pouch cells charged at 3C and 5C, respectively. Therefore, the MHD-induced suppression of lithium plating increases with C-rate, supporting the capacity gain observations vs. C-rate (Figure 2C).

3.2. Post-mortem mass and thickness analysis.

The graphite anodes from the pouch cells used for fast charging experiments were safely extracted in a glovebox. The measured film thicknesses were $137 \pm 0.1 \mu\text{m}$ for the pristine anode, $163 \pm 0.1 \mu\text{m}$ for 3C without field, $160 \pm 0.1 \mu\text{m}$ for 3C with the field, $174 \pm 0.1 \mu\text{m}$ for 5C without field and $173 \pm 0.1 \mu\text{m}$ for 5C with the field. Fast charging of the cells leads to an increase in the anode thicknesses. However, fast charging under magnetic field led to smaller increase in anode thickness of $3 \mu\text{m}$ for the 3C and $1 \mu\text{m}$ for the 5C charging rate.

3.3. Microstructural evolution of interfacial degradation.

Field emission scanning electron microscopy (FE-SEM) micrographs with Energy Dispersive X-ray Spectroscopy (EDS) scans of the extracted anodes are presented in Figure 3. Red and green dotted ellipses are used to denote regions of degradations and improvements, respectively. In Figure 3A, the backscattered electron (BSE) micrograph of anode charged at 3C without field sample shows a uniform and dense film covering the underlying graphite anode layer. A higher

magnification micrograph (Figure 3B) shows a woven mesh-like interconnected network composed of 1 – 5 μm long whiskers (or dendrites) of metallic lithium, covered by a thin film of a non-conductive SEI layer. This electrically insulating layer creates a bright contrast in the BSE micrograph against the conductive graphite background. The micrograph indicated that both the SEI and lithium dendrite network on 3C-no field sample covered the graphite anode.

Figures 3C and 3D show the micrographs of anodes from pouch cells charged at 3C and under an applied field. The images reveal a more porous interfacial film than 3C-no field at low magnification. The surface of the anode is observed to be partially covered by lithium dendritic deposition with areas of uncovered graphite particles. The deposited lithium is visibly less than 3C-no field, indicating reduced film deposition (Figure 3D). Therefore, the MHD effect limit the degradation mechanisms, in particular lithium plating, in the 3C-field sample.

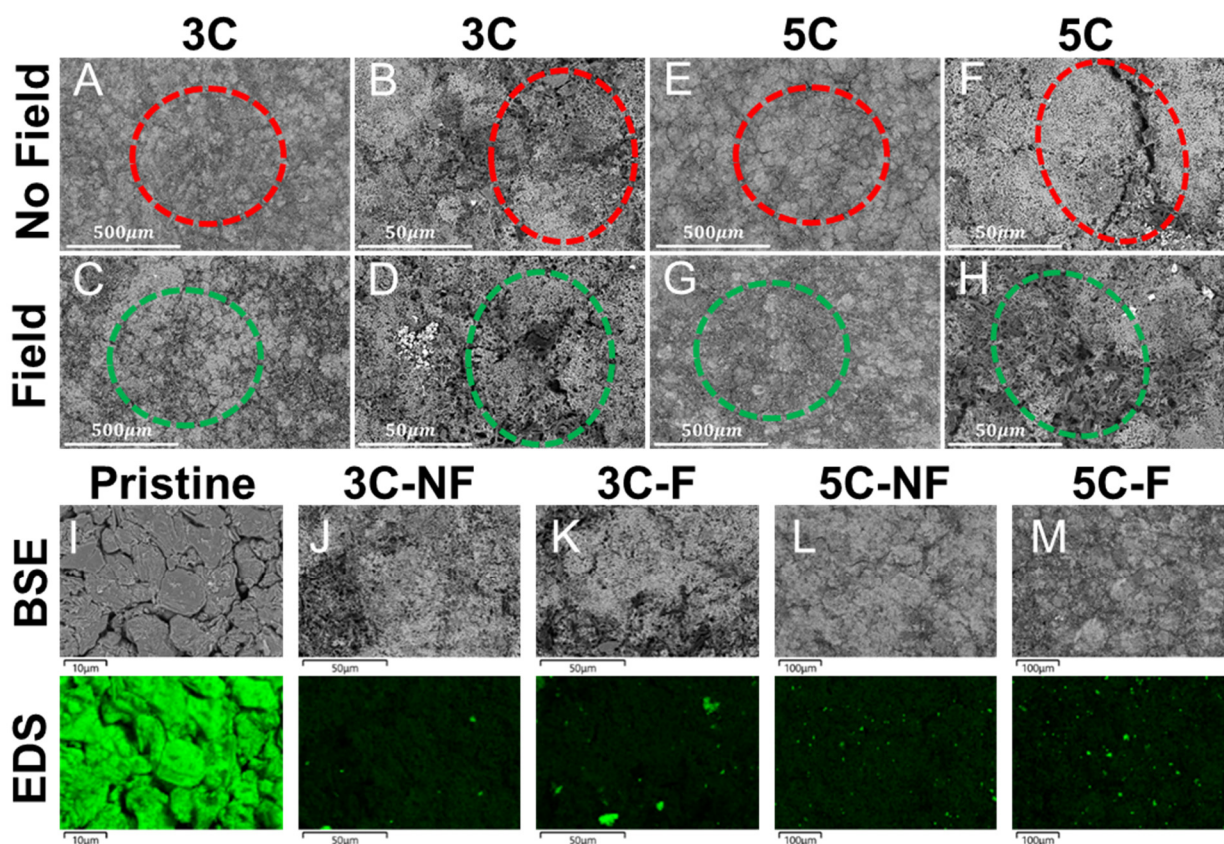


Figure 3. SEM and EDS analyses of anodic interfacial evolution subject to fast charging under the influence of magnetic field. (A and B) SEM images of 3C pouch cells without magnetic field, at magnification of 100× (A) and 1000× (B). (C and D) SEM images of 3C pouch cells with magnetic field, at magnification of 100× (A) and 1000× (B). (E and F) SEM images of 5C pouch cells without magnetic field, at magnification of 100× (E) and 1000× (F). (G and H) SEM images of 5C pouch cells with magnetic field, at magnification of 100× (G) and 1000× (H). (I to M) Backscattered (BSE) SEM and respective C K1 α EDS mapping for pristine graphite anode (I), 3C without magnetic field (J), 3C with magnetic field (K), 5C without magnetic field (L), and 5C with magnetic field (M).

Similar magnification micrographs for the 5C samples charged without and with field are shown in Figures 3E and 3F. The low magnification BSE micrograph (Figure 3E) for the 5C-no field sample show a dense deposition of the plated film on the anode surface with no visible indication of the graphite layer below. An interesting observation in the 5C-no field sample is that the interfacial film was fractured with evident cracks (Figure 3F). The film cracks on the 5C-no field anode surface are due to the volumetric strains associated with rapid lithiation at higher charging rates. At high C-rates, the non-homogenous lithium flux creates hotspots of large lithium concentrations at the anode surface. These locations exhibit rapid expansion of the graphite electrode due to rapid lithiation, consequently leading to pre-crack formations. Over multiple cycles, these cracks join and the film surface fractures to release the strain energy, exposing the underlying graphite material. The exposed graphite surface gets immediately passivated by electrolyte reduction and SEI formation, leading to consumption of active lithium and incur cell capacity loss. Fast charging of the cells under magnetic field leads to considerably more porous film network as observed on the 5C-field anodes (Figure 3G) than the 5C-no field sample.

Surprisingly, a full suppression in the interfacial fracture was observed in the film covering the 5C-with field anode sample (Figures 3G and 3H). The MHD induces mini vortices which homogenizes the lithium flux at the anode surface, consequently suppressing the locations of stress concentration and pre-crack formation. These results indicate that fast-charging under magnetic field reduces the magnitude of plated lithium and minimizes the film fracture, thereby limiting capacity loss.

EDS analysis was performed on the anode interfacial film to support the FE-SEM observations. Although lighter elements like lithium are not easily detected using EDS, the elemental mapping of carbon (C $k_{1\alpha}$, shown as green color in the maps) was used as comparative platform to gain insights into the changes in the composition of the graphite anode. Anodes with thick SEI and metallic lithium films are expected to show little or no carbon. EDS map of the pristine graphite anode with no lithium film deposition shown in Figure 3I, indicate complete carbon coverage. EDS maps of the 3C-no field and 5C-no field shown in Figures 3J and 3L, have lesser distribution of carbon in comparison to 3C-field and 5C-field anodes shown in Figures 3K and 3M, respectively. Both the EDS maps and SEM micrographs show a reduced deposition of the degradation films on the anodes that were fast-charged under a magnetic field. The results indicate that the substantial increase in the capacity gain (Figure 2C) for the 3C-field and 5C-field samples result from reduced lithium plating and minimized film cracking.

3.4. Compositional analysis of degradation film.

X-ray photoelectron spectroscopy (XPS) survey spectra were obtained for the pristine anode and samples charged at 3C and 5C (with and without applied field) at the surface (etch = 0 s) and film interior (etch = 15 s) (Figure S2). Since the pouch cells were fully discharged before disassembly, the XPS spectra's lithium signal is primarily from the deposited film rather than the intercalated

lithium in the anode. The etching process removes the top surface layer with 1s of etching removes ~1 nm of material. The plated lithium dendrites are typically covered with SEI layer (electrolytic reduction salt layer) as soon as the anodic potential becomes positive (after end-of-charging). This layer has a mixed lithium salt composition, including Li complexes with ethylene/propylene carbonates (present as solvent within the electrolyte). The organic layer is concentrated at the top due to density difference from inorganic species. This is the primary C1s signal at etch = 0s. With increased etching, the top organic layer is ablated. Some chemical changes are also incurred, thus reducing the C1s quantification.

Relative lithium content in the film covering different anodes was estimated from the XPS data to identify the influence of charging rates and magnetic field on film chemistry and composition. The survey spectra deconvolution of the film in Table 1 show a reduced lithium content for the samples charged with magnetic field, compared with samples charged without magnetic field at the same charging rates. As a reference XPS survey was performed on a pristine graphite anode that was slow charged at C/20 (Figure S2A and Table 1), showing a lower lithium and a larger carbon content compared to the fast charged samples. Figures S2B and S2C show that the surface and interior lithium compositions on the 5C-field anodes were lower by 9.2% and 24.1%, respectively, compared to 5C-no field. The reduction of lithium content on the surface of the 5C-field samples (Figure S2C) is likely a consequence of the suppression of the film cracking seen in SEM images (Figure 3). Similar observations are made where the lithium content on the surface and interior of the 3C-field samples are reduced by 20.6% and 13.9%, respectively, compared to those of the 3C-no field samples (Figures S2D and S2E). Therefore, the Li 1s in the film (Table 1, after etching) reduced in concentration by 13.9% and 24.1% on application of magnetic field at 3C and 5C, respectively. These results demonstrated a close correlation with the capacity gain

measurements of 12% and 22% at 3C and 5C, respectively. In general, the lower lithium content in the film covering anode indicates decreased lithium loss due to plating and consequent capacity gain during charging under magnetic field.

Table 1. XPS spectra elemental deconvolution for pouch cells charged with and without magnetic field.

| Spectra | Position (eV) | Atomic concentration % | | | | |
|---------|---------------|------------------------|-------|-------|-------|-------|
| | | Pristine | 3C-NF | 3C-F | 5C-NF | 5C-F |
| Li 1s | 58 | 25.32 | 48.55 | 41.72 | 51.04 | 38.75 |
| C 1s | 287 | 42.73 | 6.64 | 7.57 | 5.00 | 8.61 |
| N 1s | 400 | 0.00 | 0.33 | 0.72 | 0.39 | 0.00 |
| O 1s | 535 | 10.44 | 17.82 | 16.35 | 17.01 | 15.08 |
| F 1s | 689 | 21.00 | 25.00 | 31.82 | 25.17 | 34.83 |
| P 2p | 140 | 0.51 | 1.65 | 1.59 | 1.38 | 2.39 |

The deconvolutions of the Li 1s and C 1s spectra for the pristine, and Li 1s spectra for the 3C (field/no field) and 5C (field/no field) are shown in Figure 4. The XPS results of the atomic (narrow) spectra are primarily from the film surface, composed mostly of the SEI containing salts. A deconvolution performed on the Li 1s spectra shows peaks in the vicinity of 58 eV and 54.5 eV, corresponding to the electrolyte (LiPF_6)³³ and lithium metal³⁴, respectively. The peaks for the SEI (composed primarily of LiF, Li_2CO_3 and Li_2O) and electrolyte decomposition species, were located in the vicinity of 56 eV^{35,36}. Co 3p peaks are observed in the Li 1s spectra for the pristine and 3C-field samples due to possible cathode contamination during dismantling process. No magnetism is expected from Li_xCoO_2 contamination due to paramagnetic behavior and insignificant magnetic susceptibility of the same at room temperature³⁷. The C 1s peak was

deconvoluted into graphite (284.5 eV³⁸), C-O (286 eV³⁹) and O-C=O (288 eV³⁹). The graphite peak was fitted with a left biased and Gaussian dominant profile with the center at 284.5 eV³⁸.

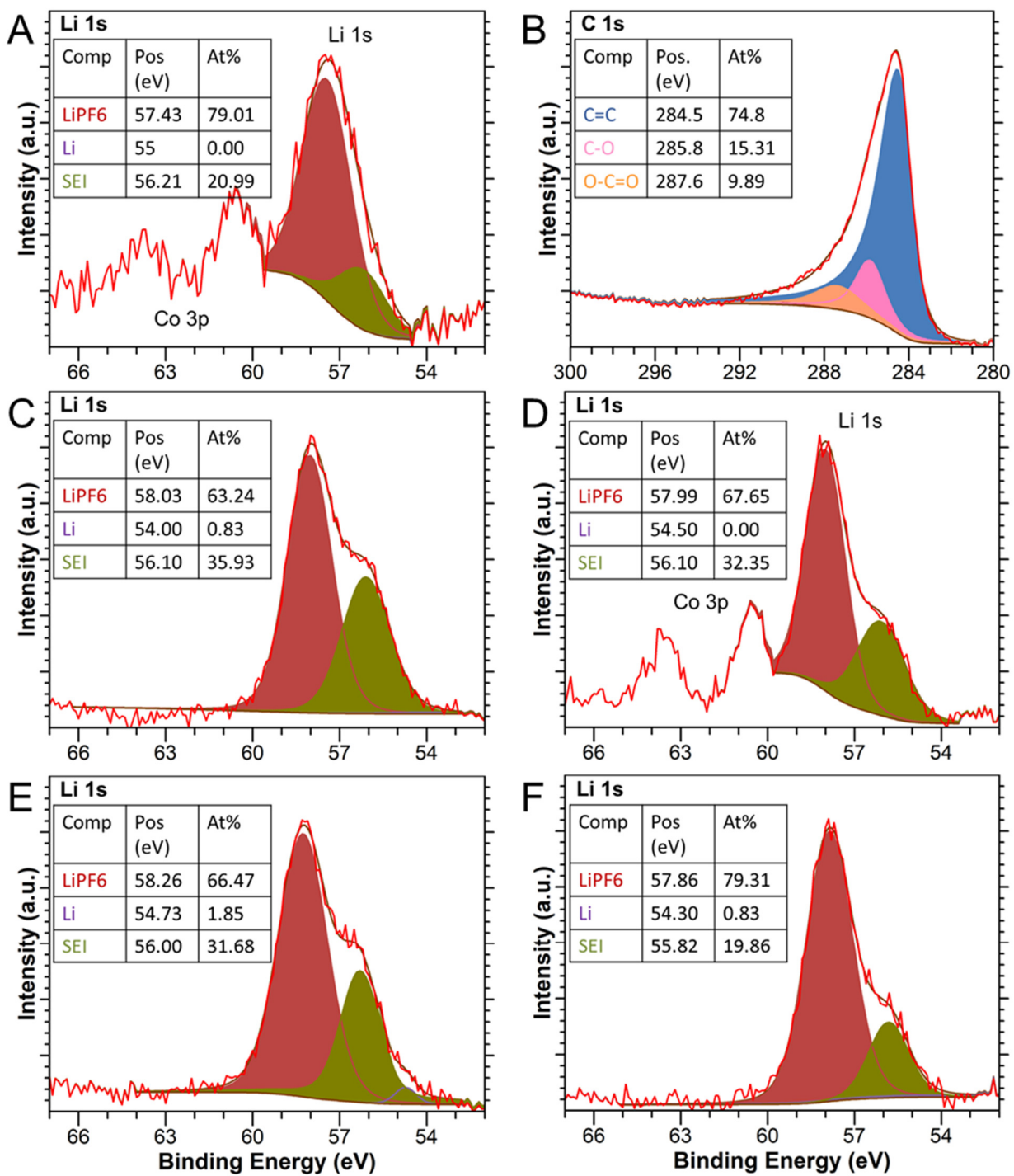


Figure 4. XPS chemical analysis of interfacial evolution influenced by magnetic field. (A and B) Atomic spectra deconvolution of pristine graphite anode Li 1s (A) and C 1s (B). (C and D) Li 1s atomic spectra deconvolution of 3C charged samples without field (C) and with field (D). (E and F) Li 1s atomic spectra deconvolution of 5C charged samples without field (E) and with field (F).

The deconvolution of the Li 1s spectrum (Figure 4A) of the pristine anode sample revealed a film composed primarily of electrolyte (79 at.% Li), followed by SEI (21 at.% Li). No trace of metallic lithium is observed in the peak fit analysis. Fitting the C 1s spectrum (Figure 4B) indicated a dominant graphite peak (75 at.% C) with the remainder as composition of species from electrolyte/SEI. For the samples charged at 3C and 5C (Figures 4C – 4F), the XPS analysis showed a reduction in the SEI and metallic lithium with the application of magnetic field. At 3C (Figures 4C and 4D), the application of magnetic field completely suppressed the lithium metal peak in the Li 1s spectrum, indicating a dominant SEI growth as a film over the metallic lithium and suppression of the plating mechanism. At 5C (Fig. 4E and 4F), the metallic lithium peak got reduced by 55.14%. Finally, the SEI peak reduced by 9.96% and 37.31% for the 3C and 5C samples with applied field, respectively.

3.5. Field strength effect on degradation.

From Equation 1, it would be expected that increasing the magnetic field strength (B) should also improve electrochemical performance due to larger MHD forces (F_{MHD}). Therefore, the pouch cells were charged at 3C and 5C over 10 cycles under magnetic field strengths of 0, 1.2, 1.8 and 3.1 kG, to investigate the influence of magnetic field strength on interfacial degradation. The discharge capacity increases with magnetic field from 0 to 1.8 kG, approaches a maximum and saturates beyond that magnitude (Figure 5A). The improvement in capacity is supported by a rise in coulombic efficiency and ΔDCR measurements with field strength, indicating a reduced lithium

loss (Figures 5B and 5C). The improvement in the coulombic efficiency can be inferred to as a lower electrochemical degradation at the end of each charge cycle. The reduction in the ΔDCR loss (Figure 5C) confirmed a reduction in the conductive lithium deposition with increment in the applied field strength. The effect is more dominant at 5C compared to 3C (Figure S3), an observation similar to electrochemical and SEM analysis (Figures 2 and 3). For the pouch cells used in the present analysis, the influence of field strength on electrochemical performance saturated near ~ 2 kG. Although the Lorentz force will increase with magnetic field (B), no further influence on the anode damage mechanisms occurs because the saturation indicates a peak in the homogenization effect of the convective ionic flux by the MHD forces. The degradation observed at the highest magnetic fields could be a consequence of large but homogenized ionic transport at the anode/separator interface. The peak in the magnetic field effect is beneficial in minimizing the cost of the magnetic field-based interventions. It indicates that magnetic field strength produced with permanent magnets or small electromagnet coils is enough to maximize the MHD forces' impact in enhancing battery performance.

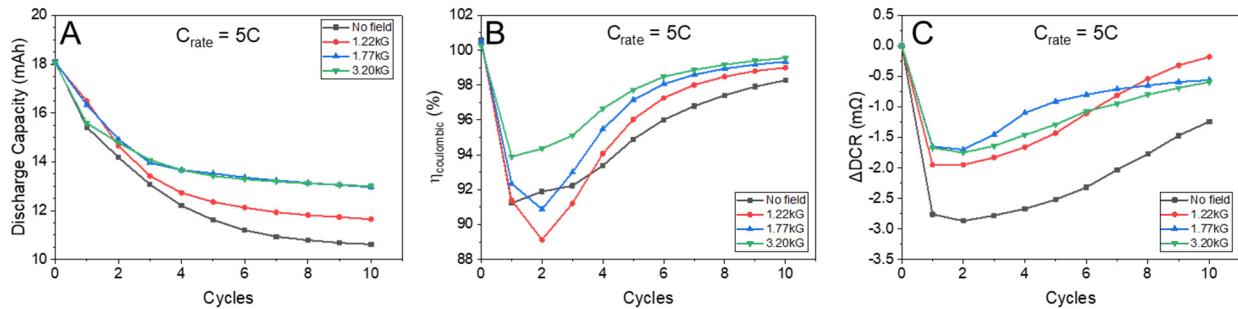


Figure 5. Effect of varying magnetic field strengths on the electrochemical performance for pouch cells charged at 5C and 10 cycles. (A) Discharge capacity measurement. (B) Coulombic efficiency. (C) DC Resistance measurement.

Further enhancement of performance may be possible via incorporating magnetic elements to the electrode composition. Low tortuosity electrodes⁴⁰ would not only enhance capacity of the battery but also improve ionic transport. This would further minimize degradation during fast charging, especially under applied magnetic field. For larger format cell applications, design modification could be done to accommodate an EM or permanent magnet next to the battery assembly with the electronics shielded from the EM flux. Future works would include these design modifications and large format cells will be tested with different magnetic field sources (AC, DC, pulsed, etc.) and charging protocols to maximize the electrochemical performance.

4. CONCLUSIONS

In this work, we have demonstrated the application of magneto-electrochemical interactions in commercial lithium-ion batteries with graphite anodes to significantly improve their performance and cycle life during fast charging. This improvement results from the homogenization of transversely diffusing ionic flux at the anode/separator interface by Lorentz forces via the MHD effect. The homogenized lithium flux minimized the irregular localized concentration hot spots on the anode surface. Consequently, degradation mechanisms, like lithium plating, SEI growth and film fracture, on the anode surface were minimized. An improvement in the discharge capacity was observed upon application of magnetic field on LCO/C pouch cells, with capacity gain increasing with C-rate up to a maximum of ~22% at 5C charging rate. *In-situ* DCR measurements indicated a reduced lithium deposition due to the application of magnetic field, which was validated via post-mortem thickness, FE-SEM/EDS and XPS analyses. A reduced film thickness was observed, notably at 3C, for the samples charged under magnetic field. The FE-SEM micrographs revealed that film deposited on anodes charged at 5C charging rates was covered with cracks but no cracking was observed for films on anode charged at 5C under magnetic field. The

EDS analysis of the C peak confirmed a depreciation in the plating intensity with field. A reduced lithium content was estimated from the surface and etched XPS analysis of the magnetic field applied fast charging lithium pouch cells. The deconvolution of the XPS survey spectra estimated a reduction in the lithium content for the 5C and 3C samples by 24.1% and 13.9%, respectively. These results were closely consistent with the capacity gain measurements. It was also observed that capacity gain with increasing strength of the applied magnetic field saturates – a consequence of reaching a maximum in the homogenization of the lithium flux at the anode surface due to the applied magnetic field. The electromagnet technology can be integrated in an EV battery design and be engaged at the charging stations during fast charging.

SUPPORTING INFORMATION

- Figures showing magnetic field effects on electrochemical cycling parameters with varying C-rate and temperature of cycling.
- Figures of XPS survey spectra with deconvolution for chemical analysis of pristine samples, etched/unetched samples and samples charged with/without magnetic field.
- Figures showing the effects of magnetic field strength variation on electrochemical cycling parameters at 3C charging rate.

AUTHOR INFORMATION

Corresponding Author

*Email: nlebedim@ameslab.gov.

Author Contributions

A.S. contributed towards Investigation, Methodology, Formal analysis, Visualization, Writing - original draft, Writing - review & editing. I.C.N. contributed towards Supervision, Formal analysis, Investigation, Writing - review & editing, Funding acquisition. P.S. contributed towards Supervision, Formal analysis, Writing - review & editing, Investigation.

Funding Sources

This work was supported by the U.S. Department of Energy, Laboratory Directed Research and Development (LDRD) program at Ames Laboratory. Ames Laboratory is operated for the U.S. Department of Energy by Iowa State University of Science and Technology under Contract No. DE-AC02-07CH11358.

ACKNOWLEDGEMENT

The authors thank Dr. Matthew Lynn for acquiring the SEM and EDS maps.

REFERENCES

- (1) Goodenough, J. B.; Park, K.-S. The Li-Ion Rechargeable Battery: A Perspective. *J. Am. Chem. Soc.* **2013**, *135* (4), 1167–1176. <https://doi.org/10.1021/ja3091438>.
- (2) Zu, C.-X.; Li, H. Thermodynamic Analysis on Energy Densities of Batteries. *Energy Environ. Sci.* **2011**, *4* (8), 2614. <https://doi.org/10.1039/c0ee00777c>.
- (3) Etacheri, V.; Marom, R.; Elazari, R.; Salitra, G.; Aurbach, D. Challenges in the Development of Advanced Li-Ion Batteries: A Review. *Energy Environ. Sci.* **2011**, *4* (9), 3243. <https://doi.org/10.1039/c1ee01598b>.
- (4) Chen, J. *Graphite, Silicon, Metal, and Other Anode Materials for Motive Lithium-Ion*

Batteries: Global Market and Emerging Opportunities; Massachusetts, 2020.
https://www.reportlinker.com/p05843528/?utm_source=PRN.

- (5) Liu, Q.; Du, C.; Shen, B.; Zuo, P.; Cheng, X.; Ma, Y.; Yin, G.; Gao, Y. Understanding Undesirable Anode Lithium Plating Issues in Lithium-Ion Batteries. *RSC Adv.* **2016**, *6* (91), 88683–88700. <https://doi.org/10.1039/C6RA19482F>.
- (6) Dey, A. N.; Sullivan, B. P. The Electrochemical Decomposition of Propylene Carbonate on Graphite. *J. Electrochem. Soc.* **1970**, *117* (2), 222. <https://doi.org/10.1149/1.2407470>.
- (7) Peled, E. The Electrochemical Behavior of Alkali and Alkaline Earth Metals in Nonaqueous Battery Systems—The Solid Electrolyte Interphase Model. *J. Electrochem. Soc.* **1979**, *126* (12), 2047. <https://doi.org/10.1149/1.2128859>.
- (8) Peled, E.; Golodnitsky, D.; Ardel, G. Advanced Model for Solid Electrolyte Interphase Electrodes in Liquid and Polymer Electrolytes. *J. Electrochem. Soc.* **1997**, *144* (8), L208–L210. <https://doi.org/10.1149/1.1837858>.
- (9) Aurbach, D.; Markovsky, B.; Levi, M. .; Levi, E.; Schechter, A.; Moshkovich, M.; Cohen, Y. New Insights into the Interactions between Electrode Materials and Electrolyte Solutions for Advanced Nonaqueous Batteries. *J. Power Sources* **1999**, *81–82*, 95–111. [https://doi.org/10.1016/S0378-7753\(99\)00187-1](https://doi.org/10.1016/S0378-7753(99)00187-1).
- (10) Winter, M. The Solid Electrolyte Interphase – The Most Important and the Least Understood Solid Electrolyte in Rechargeable Li Batteries. *Zeitschrift für Phys. Chemie* **2009**, *223* (10–11), 1395–1406. <https://doi.org/10.1524/zpch.2009.6086>.
- (11) Verma, P.; Maire, P.; Novák, P. A Review of the Features and Analyses of the Solid

- Electrolyte Interphase in Li-Ion Batteries. *Electrochim. Acta* **2010**, *55* (22), 6332–6341.
<https://doi.org/10.1016/j.electacta.2010.05.072>.
- (12) Vetter, J.; Novák, P.; Wagner, M. R.; Veit, C.; Möller, K.-C.; Besenhard, J. O.; Winter, M.; Wohlfahrt-Mehrens, M.; Vogler, C.; Hammouche, A. Ageing Mechanisms in Lithium-Ion Batteries. *J. Power Sources* **2005**, *147* (1–2), 269–281.
<https://doi.org/10.1016/j.jpowsour.2005.01.006>.
- (13) von Lüders, C.; Zinth, V.; Erhard, S. V.; Osswald, P. J.; Hofmann, M.; Gilles, R.; Jossen, A. Lithium Plating in Lithium-Ion Batteries Investigated by Voltage Relaxation and in Situ Neutron Diffraction. *J. Power Sources* **2017**, *342*, 17–23.
<https://doi.org/10.1016/j.jpowsour.2016.12.032>.
- (14) Solchenbach, S.; Pritzl, D.; Kong, E. J. Y.; Landesfeind, J.; Gasteiger, H. A. A Gold Micro-Reference Electrode for Impedance and Potential Measurements in Lithium Ion Batteries. *J. Electrochem. Soc.* **2016**, *163* (10), A2265–A2272. <https://doi.org/10.1149/2.0581610jes>.
- (15) An, S. J.; Li, J.; Daniel, C.; Kalnaus, S.; Wood, D. L. Design and Demonstration of Three-Electrode Pouch Cells for Lithium-Ion Batteries. *J. Electrochem. Soc.* **2017**, *164* (7), A1755–A1764. <https://doi.org/10.1149/2.0031709jes>.
- (16) Smith, A. J.; Burns, J. C.; Dahn, J. R. A High Precision Study of the Coulombic Efficiency of Li-Ion Batteries. *Electrochem. Solid-State Lett.* **2010**, *13* (12), A177.
<https://doi.org/10.1149/1.3487637>.
- (17) Downie, L. E.; Krause, L. J.; Burns, J. C.; Jensen, L. D.; Chevrier, V. L.; Dahn, J. R. In Situ Detection of Lithium Plating on Graphite Electrodes by Electrochemical Calorimetry. *J.*

- Electrochem. Soc.* **2013**, *160* (4), A588–A594. <https://doi.org/10.1149/2.049304jes>.
- (18) Burns, J. C.; Stevens, D. A.; Dahn, J. R. In-Situ Detection of Lithium Plating Using High Precision Coulometry. *J. Electrochem. Soc.* **2015**, *162* (6), A959–A964. <https://doi.org/10.1149/2.0621506jes>.
- (19) Tran, T.; Kinoshita, K. Lithium Intercalation/Deintercalation Behavior of Basal and Edge Planes of Highly Oriented Pyrolytic Graphite and Graphite Powder. *J. Electroanal. Chem.* **1995**, *386* (1–2), 221–224. [https://doi.org/10.1016/0022-0728\(95\)03907-X](https://doi.org/10.1016/0022-0728(95)03907-X).
- (20) Zhang, X.; Sastry, A. M.; Shyy, W. Intercalation-Induced Stress and Heat Generation within Single Lithium-Ion Battery Cathode Particles. *J. Electrochem. Soc.* **2008**, *155* (7), A542--A552.
- (21) Laresgoiti, I.; Käbitz, S.; Ecker, M.; Sauer, D. U. Modeling Mechanical Degradation in Lithium Ion Batteries during Cycling: Solid Electrolyte Interphase Fracture. *J. Power Sources* **2015**, *300*, 112–122. <https://doi.org/10.1016/j.jpowsour.2015.09.033>.
- (22) Deshpande, R. D.; Bernardi, D. M. Modeling Solid-Electrolyte Interphase (SEI) Fracture: Coupled Mechanical/Chemical Degradation of the Lithium Ion Battery. *J. Electrochem. Soc.* **2017**, *164* (2), A461–A474. <https://doi.org/10.1149/2.0841702jes>.
- (23) Sarkar, A.; Nlebedim, I. C.; Shrotriya, P. Performance Degradation Due to Anodic Failure Mechanisms in Lithium-Ion Batteries. *J. Power Sources* **2020**, 229145. <https://doi.org/10.1016/j.jpowsour.2020.229145>.
- (24) Sarkar, A.; Shrotriya, P.; Chandra, A. Modeling of Separator Failure in Lithium-Ion Pouch Cells under Compression. *J. Power Sources* **2019**, *435*, 226756.

<https://doi.org/10.1016/j.jpowsour.2019.226756>.

- (25) Molokov, S.; Moreau, R.; Moffat, H. K. Magnetohydrodynamics Historical Evolution and Trends. *Appl. Math. Comput.* **1996**, *80* (2–3), i–ii.
- (26) Aaboubi, O.; Chopart, J. P.; Douglade, J.; Olivier, A.; Gabrielli, C.; Tribollet, B. Magnetic Field Effects on Mass Transport. *J. Electrochem. Soc.* **1990**, *137* (6), 1796–1804. <https://doi.org/10.1149/1.2086807>.
- (27) Tacke, R. A.; Janssen, L. J. J. Applications of Magneto-electrolysis. *J. Appl. Electrochem.* **1995**, *25* (1) 1–5. <https://doi.org/10.1007/BF00251257>.
- (28) Dong, J.; Dai, H.; Wang, C.; Lai, C. Uniform Lithium Deposition Driven by Vertical Magnetic Field for Stable Lithium Anodes. *Solid State Ionics* **2019**, *341*, 115033. <https://doi.org/10.1016/j.ssi.2019.115033>.
- (29) Shen, K.; Wang, Z.; Bi, X.; Ying, Y.; Zhang, D.; Jin, C.; Hou, G.; Cao, H.; Wu, L.; Zheng, G.; Tang, Y.; Tao, X.; Lu, J. Magnetic Field-Suppressed Lithium Dendrite Growth for Stable Lithium-Metal Batteries. *Adv. Energy Mater.* **2019**, *9* (20), 1900260. <https://doi.org/10.1002/aenm.201900260>.
- (30) Costa, C. M.; Merazzo, K. J.; Gonçalves, R.; Amos, C.; Lanceros-Méndez, S. Magnetically Active Lithium-Ion Batteries towards Battery Performance Improvement. *iScience* **2021**, *24* (6), 102691. <https://doi.org/10.1016/j.isci.2021.102691>.
- (31) Huizhou Markyn New Energy Co., L. *Lithium Battery UN38.3 Test Report*; 2017.
- (32) Harter, J.; McIntyre, T. J.; White, J. D. *Electrical Safety Practices Developed for Automotive*

- Lithium Ion Battery Dismantlement*; Oak Ridge, TN (United States), 2020.
<https://doi.org/10.2172/1606888>. <https://www.osti.gov/biblio/1606888/>
- (33) Dedryvère, R.; Leroy, S.; Martinez, H.; Blanchard, F.; Lemordant, D.; Gonbeau, D. XPS Valence Characterization of Lithium Salts as a Tool to Study Electrode/Electrolyte Interfaces of Li-Ion Batteries. *J. Phys. Chem. B* **2006**, *110* (26), 12986–12992. <https://doi.org/10.1021/jp061624f>.
- (34) Wood, K. N.; Teeter, G. XPS on Li-Battery-Related Compounds: Analysis of Inorganic SEI Phases and a Methodology for Charge Correction. *ACS Appl. Energy Mater.* **2018**, *1* (9), 4493–4504. <https://doi.org/10.1021/acsaem.8b00406>.
- (35) Grissa, R.; Fernandez, V.; Fairley, N.; Hamon, J.; Stephant, N.; Rolland, J.; Bouchet, R.; Lecuyer, M.; Deschamps, M.; Guyomard, D.; Moreau, P. XPS and SEM-EDX Study of Electrolyte Nature Effect on Li Electrode in Lithium Metal Batteries. *ACS Appl. Energy Mater.* **2018**, *1* (10), 5694–5702. <https://doi.org/10.1021/acsaem.8b01256>.
- (36) Parimalam, B. S.; Lucht, B. L. Reduction Reactions of Electrolyte Salts for Lithium Ion Batteries: LiPF₆, LiBF₄, LiDFOB, LiBOB, and LiTFSI. *J. Electrochem. Soc.* **2018**, *165* (2), A251–A255. <https://doi.org/10.1149/2.0901802jes>.
- (37) Hertz, J. T.; Huang, Q.; McQueen, T.; Klimczuk, T.; Bos, J. W. G.; Viciu, L.; Cava, R. J. Magnetism and Structure of Li_xCoO₂ and Comparison to Na_xCoO₂. *Phys. Rev. B* **2008**, *77* (7), 075119. <https://doi.org/10.1103/PhysRevB.77.075119>.
- (38) Graphite <http://www.xpsfitting.com/2008/12/graphite.html>.
- (39) Carbon <https://xpssimplified.com/elements/carbon.php>.

- (40) Billaud, J.; Bouville, F.; Magrini, T.; Villevieille, C.; Studart, A. R. Magnetically Aligned Graphite Electrodes for High-Rate Performance Li-Ion Batteries. *Nat. Energy* **2016**, *1* (8) 16097.. <https://doi.org/10.1038/nenergy.2016.97>.